This is the accepted version of the paper.

This version of the publication may differ from the final published version.

1 **Aeroacoustic investigation of a ducted wind turbine employing bio-**

2 **inspired airfoil profiles**

3 Mostafa Mozafari, [1] Mahyar Sadeghi Malekabadi, [2] Amirhosein Fardi[3], Christoph Bruecker [4]
4 and Mehran Masdari [5].

5 [1] Faculty of New Sciences and Technologies, University of Tehran, Tehran, Iran.
6 [2] Faculty of Aerospace Engineering, Sharif University of Technology, Tehran, Iran.
7 [3] Faculty of Mechanical Engineering, Lakehead University, Thunder Bay, ON P7B 5E1, Canada.
8 [4,5] City, University of London, Northampton Square, London, EC1V 0HB, UK.

9 Correspondence should be addressed to Mehran Masdari; mehran.masdari@city.ac.uk

10

11 **Abstract**

12 Ducted wind turbines for residential purposes are characterized by a lower diameter with
13 respect to conventional wind turbines for on-shore applications. The noise generated by the
14 rotor plays a significant role in the overall aerodynamic noise. By making modifications to the
15 blade sections of the wind turbine, we can alter the contributions of aeroacoustic noise sources.
16 This study introduces innovative wind turbine blade designs inspired by owl wing
17 characteristics, achieving significant noise reduction without compromising aerodynamic
18 performance. A three-dimensional (3D) scan of an owl wing was first employed to derive a
19 family of airfoils. The airfoils were employed to modify the blade of a referenced wind turbine
20 airfoil section at various positions on the blade span to determine a blade operating more
21 efficiently at the tip-speed ratio of the original one. While maintaining the same aerodynamic
22 performance, the bio-inspired profiles show a more uniform pressure coefficient distribution,
23 considerably decreasing in the noise level. Furthermore, this study makes considerable
24 progress in ducted wind turbine design by obtaining an 8 dB noise reduction and a 12%
25 improvement in sound pressure level. An in-depth aerodynamic examination shows a 6.4% rise
26 in thrust force coefficient and optimized power coefficients, reaching a peak at a Tip Speed
27 Ratio (TSR) of 8, demonstrating improved energy conversion efficiency. The results highlight
28 the dual advantage of the innovative design: significant noise reduction and enhanced
29 aerodynamic efficiency, offering a promising alternative for urban wind generation.
30
31 **Keywords**: Ducted Wind Turbine, Aeroacoustics, Barn Owl, Large Eddy Simulation.

32 **Nomenclatures**

AOA	Angle of Attack	C_T	thrust force coefficient
c	Chord of Airfoil	TSR	Tip Speed Ratio
C_l	Lift Coefficient	SPL	Sound Pressure Level
C_d	Drag Coefficient	OASPL	Overall Sound Pressure Level
Cl/Cd	Lift-to-drag ratio	C_{PWR}	Power Coefficient
2D / 3D	Two / Three Dimensional	LES	Large Eddy Simulation
WT	Wind Turbine	FW-H	Ffowcs Williams-Hawkings
DWT	Ducted Wind Turbine	CFD	Computational Fluid Dynamics

33 **Introduction**

34 The effect of rising global warming has shifted the world to clean energy sources; the most
35 efficient source of clean energy is wind energy [1]. The use of such renewable energy has
36 grown rapidly [2], to the point of justifying the usage of wind turbines in profitable locations
37 in urban areas, to reduce the costs of energy delivery to the user. The integration in the urban
38 environment comes at the cost of reducing the rotor sizes of the wind turbine, by adding a duct
39 to increase the incoming flow speed lowering the effect of incoming turbulent fluctuations, and
40 having to respect more stringent aeroacoustic regulations [3].

41 The reduction of the wind turbine rotor changes the contributions of the aeroacoustic noise
42 sources, since the turbine is now operating at a relatively lower Reynolds number and at a much
43 higher rotational speed than a conventional one. In this respect, the loading and thickness
44 contributions are no longer negligible. The overall aerodynamic noise is a combination of the
45 one produced by the rotor and the one determined by the duct. While a lot of studies have
46 focused on the coupling between the duct or diffuser and the rotor, only a few have proposed
47 the use of specific airfoils for such low Reynolds number and high turbulence applications.
48 Bio-inspired airfoils have been shown to possess particular characteristics to allow birds to fly
49 in very turbulent environments, with an extremely high lift-to-drag ratio, and at the same time
50 do silently [4]. This has inspired the use of such airfoils for drones and small rotor applications.
51 Despite being known for their feather characteristics, owl's wings have an additional
52 characteristic. The high lift-to-drag ratio of the profile, allows the bird to enormously reduce
53 the flying speed to sustain the bird's weight. Combined with the additional serrated leading
54 edge, the velvety surface and the fringes at the trailing edge, the owl's wing performance is the
55 most silent in the animal kingdom in the final phase of attacking the prey [5-7]. From an
56 aerodynamic point of view the combination of the previous factors, seems to also produce a
57 more favorable and thinner boundary layer, which helps in increasing the aerodynamic
58 performance of the wing. Various studies have been performed experimentally [8, 9],
59 numerically [10-12] and in real flight [13] to use the owl wing characteristics.

60 In the realm of aerodynamics, flow and noise control are pivotal for enhancing the performance
61 and reducing the environmental impact of wind turbines. Two primary methods are employed
62 to achieve these objectives: active and passive flow control techniques. Active methods, such
63 as the use of dielectric barrier discharge plasma actuators demonstrated by Lee et al. [14],
64 actively manipulate the flow field around structures to control separation and reduce drag,
65 thereby influencing noise generation. On the other hand, passive methods involve structural
66 modifications to the body, which passively influence the flow and noise characteristics. An
67 example is the use of grooved surfaces on deflectors to improve the aerodynamic performance
68 of Savonius wind turbines, as explored by Fatahian et al. [15]. This research aligns with passive
69 flow control strategies by adopting a bio-inspired model that leverages the silent flight
70 characteristics of owl wings. The integration of airfoil profiles inspired by the natural wing
71 structure of owls represents a novel approach in the design of ducted wind turbines to passively
72 control flow and reduce noise. Such bio-inspired designs, as evidenced by the comparative
73 analysis of flow control over a circular cylinder with detached flexible and rigid splitter plates
74 by Eydi et al. [16], underscore the potential of nature-inspired solutions in engineering
75 applications. Our study builds upon this foundation, employing passive flow control through
76 bio-mimicry to achieve a harmonious balance between aerodynamic efficiency and noise
77 reduction in wind turbine design. Additionally, Song et al. [17]demonstrated that the bionic
78 edge design strategy can effectively control the turbulent flow field and effectively break down
79 airflow near the trailing edge. This leads to improved thrust and decreased noise levels.

2

80   According to the literature review in this study, it was concluded that very few studies focused
81   on isolating the airfoil characteristics and employing them for industrial applications. In a study
82   by Liu et al. [18], a laser scanner was used to scan the owl wing and characterize its geometric
83   characteristics. These characteristics included camber, chord, twist, and thickness distribution.
84   An analysis of flow interactions with surfaces and flow physics surrounding an owl airfoil was
85   conducted by Klan et al. [19]. Bachmann et al. [20] provided a comprehensive characterization
86   of the wings and feathers of barn owls in high spatial resolution. They conclude that barn owls
87   have evolved specialized wings and feathers to reduce flight noise. To investigate the wings at
88   high spatial resolution, they used confocal laser scanning microscopy, surface digitizing, and
89   computed tomography. They found that these birds of prey have huge wings relative to their
90   body mass, which enables slow flights with increased maneuverability. At low speeds, the
91   researchers found that modifications to the wings' surfaces and edges helped stabilize airflow.
92   Geyer et al. [21] conducted a comprehensive study on owl wings. In addition to performing
93   numerical calculations, they conducted laboratory tests on the wings of owls and several other
94   birds. According to their findings, an owl's wings can be 20 decibels quieter than other birds'
95   wings when gliding. This was achieved by exploiting the relatively lower speed at which the
96   owl's profile was able to operate. Kondo et al. [22] studied the aerodynamic characteristics of
97   an owl-like airfoil at a Reynolds number of 2300. Their results indicate that the deeply concave
98   lower surface of the owl-like airfoil contributes to lift augmentation, and both a round leading
99   edge and a flat upper surface lead to lift enhancement and drag reduction, determined by the
100   presence of a thin laminar separation bubble near the leading edge. Subsequently, the owl-like
101   airfoil has a higher lift-to-drag ratio than the high lift-to-drag Ishii airfoil at low Reynolds
102   number. A new airfoil for the wind turbine blades was designed and used in the wind turbine
103   blades by Tian et al. [23]. Results show that the bio-inspired airfoil inspired by the Long-eared
104   Owl's wing has a superior lift coefficient and stalling performance, and thus can enhance wind
105   turbine blade performance. An owl inspired airfoil without serrations and a Downy wing
106   surface was compared to a NACA airfoil at low Reynolds numbers by Anyoji et al. [24].
107   According to their results, the owl inspired airfoil has more lift and generally performs better
108   than the base airfoil at low Reynolds numbers. Moslem et al. [25] demonstrated that a
109   bioinspired propeller not only diminishes both harmonic and broadband noise but also achieves
110   a superior noise level compared to the baseline configuration. Aono et al. [26] investigated the
111   aerodynamics of an owl wing-like airfoil for low Reynolds numbers using numerical methods
112   and the LES turbulence model. They compared the simulation results with several conventional
113   airfoils and showed that the owl wing-inspired airfoil has a higher lift-to-drag coefficient than
114   the other airfoils compared. They reported that this increase was due to the creation of a high-
115   pressure area in the suction area of the airfoil due to the curvature of the owl airfoil.
116   Muthuramalingam et al. [27] explored laminar flow control by employing leading-edge
117   serration, demonstrating a postponement in the transition from laminar to turbulent flow. This
118   effect parallels the phenomenon observed in owl flight, contributing to further noise reduction.
119   Despite all the previous results, whether these airfoils can be reliably applied for a rotating
120   blade at low Reynolds number is still under debate. While in fact the aspect ratio is very similar,
121   the loading distribution of a rotating blade is relatively different from the distribution of a bird's
122   wing in gliding conditions.

123   In this manuscript, an investigation is made to study how bio-inspired airfoils could be
124   employed to outperform the loading distribution of a rotating blade. The study proceeds by
125   evaluating how the aerodynamic performance would affect the aeroacoustic footprint of the
126   rotor, including loading and thickness noise and discussing the broadband part due to the
127   change in boundary layer characteristics. The manuscript is organized as follows: In section 2
128   of this research, a family of airfoils is produced through 3D scanning. These airfoils are then

129 utilized in the design of ducted wind turbine blades, as detailed in section 3. The following
130 sections present a comprehensive numerical analysis of cases (benchmark and multi-section
131 blades), along with the results of aerodynamic and aeroacoustic prediction.

132 **Airfoil family generation**

133 To generate a family of bio-inspired airfoils, a taxidermy owl as shown in Figure 1 has been
134 placed in the center of a 3D scanner. Circular targets mark the owl wing to allow for combining
135 multiple fields of view in a unique 3D reconstruction. In this test, the Solutionix
136 C500-Structured Light 3D Scanner has been used, with a final reconstruction accuracy of 0.01
137 mm. The center points of the wing are relatively less accurate, due to possible errors induced
138 by the presence of the velvet surface and the feathers.

139 Illustrated below is the barn owl wing alongside its corresponding reverse model (Figure 2).
140 The airfoil sections exhibit varying airfoil shapes and chord lengths. The data fitting procedure
141 involved using MATLAB to employ Polynomial fitting. For both the upper and lower surfaces
142 of the airfoil, an independent polynomial of degree six was selected. Figure 3 provides an
143 illustrative instance featuring the root airfoil, offering a visualization of its equations and the
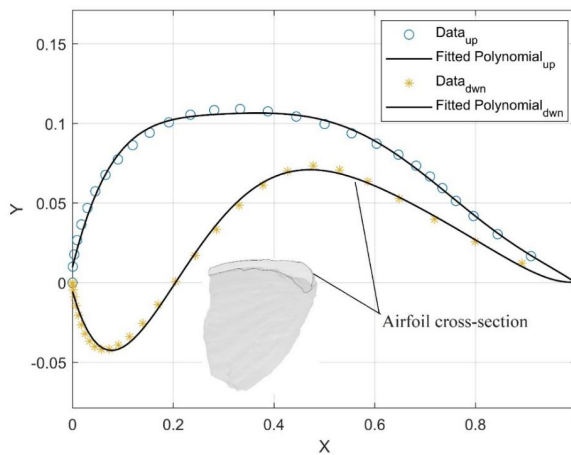144 associated fitting curve.
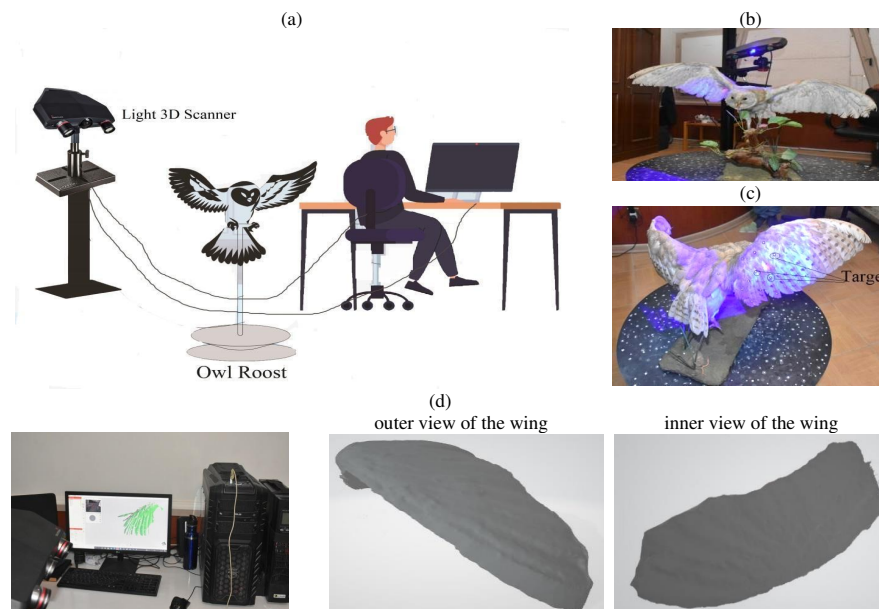
145 Figure 1: the experimental set-up. (a) A general illustration of the experimental setup. (b) An owl with the
146 camera laser (c) A close view of the laser light sheet with targets on the owl wing (d) 3-D scan output of the
147 owl's wing.

4

(a)   (b)

148   Figure 2: (a) Barn owl wing, (b) inverted owl wing model.

149

150   Figure 3: Fitting Results for Airfoil Profile.

151   The extracted airfoil exhibits a maximum thickness of 12% at x/c=0.11. In the study by Klan
152   et al. [19], these characteristics are documented as 14.77% and 0.15, respectively. It's important
153   to acknowledge a slight variance in the airfoil's overall specifications, potentially stemming
154   from the owl's taxidermy process and water loss from the bird's body. Furthermore, the airfoil
155   features a cusp-type trailing edge, consistent with the research of Ricks et al. [28], which
156   suggests that such a slender trailing edge is associated with reduced noise generation. As
157   indicated, the spatial arrangement of the upper and lower airfoil surfaces has been
158   approximated using a 6th degree polynomial function. This function, denoted as
159   $y_c = ax^6 + bx^5 + cx^4 + dx^3 + ex^2 + fx + g$, has coefficients detailed in Table 1. Here, 'x' represents
160   the positional coordinates along the direction of the airfoil chord.

161   Table 1: Polynomial Coefficients for Geometric Approximation of Airfoil Surfaces.

Type	a	b	c	d	e	f	g
upper surface	-6.62	23	-30.77	20.1	-6.98	1.266	0.01
lower surface	7.76	-28.33	41.31	-29.72	10.10	-1.1	-0.0056

162 **Blade Design**

163 After scanning the owl's wing, as depicted in Figure 4, a comprehensive numerical analysis
164 was conducted in the vicinity of the owl's wing across a range of frequencies. The simulation
165 was carried out using ANSYS-FLUENT software, employing the LES turbulence model and
166 FW-H acoustic analogy. The domain is subjected to boundary conditions, with velocity inlet
167 and pressure outlet. Additionally, a symmetry condition is applied to surface included the wing
168 root. The computational domain had dimensions of 0.5 * 0.8 * 2 meters, with a mesh count of
169 0.5 million. Based on sound pressure level measurements conducted by Gruschka et al. [29], it
170 was established that the owl's sound remains inaudible beyond a 3-meter distance for
171 frequencies below 2000 Hz. Consequently, it was decided to incorporate SPL contour tuned to
172 frequencies of 500, 1000, 1600, and 2000 Hz. Moreover, a recurring pattern can be observed
173 across different frequencies in all four cases. Additionally, the following section presents the
174 OASPL curve for the wing sections along the span direction. Upon examination of this curve,
175 it became evident that specific locations along the span of the owl's wing consistently exhibited
176 lower noise levels compared to others. Consequently, these positions were selected as the
177 preferred locations for airfoil extraction. In the selection of these positions, careful
178 consideration was given to choose justifiable points within the range. These positions were
179 identified at 3%, 12.5%, 27%, 44%, and 68% of the owl wing's span, respectively. The
180 reduction in noise during owl flight was attributed to the distinctive characteristics of its airfoil.
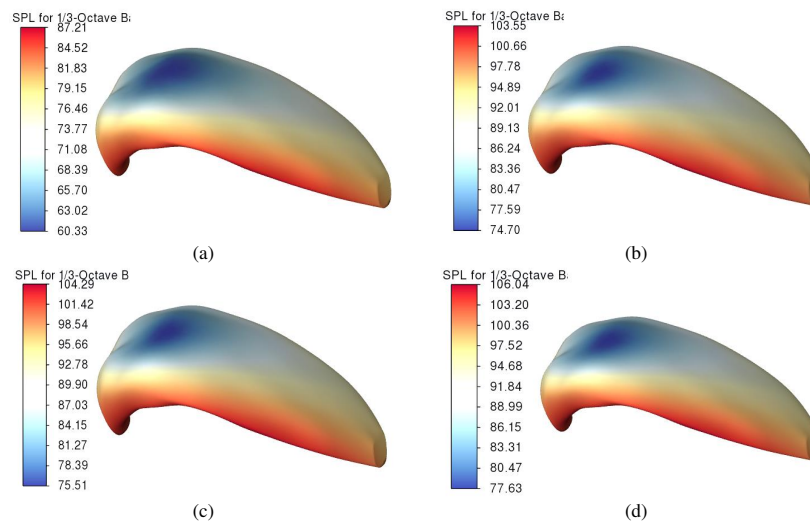

181 Figure 4: Noise level contours (a) 500 Hz, (b) 1 kHz, (c) 1.6 kHz and (d) 2 kHz.

182 In light of this discovery, as depicted in Figure 5a, the decision was made to extract and employ
183 these airfoil characteristics from the owl's wing as the preferred airfoil profiles for blade design.
184 The distribution of OASPL shows minimal variations along the owl's wingspan. Interpolation
185 has been utilized to pinpoint cross-sectional data, with selections made at intervals of 7%, 15%,
186 30%, 50%, and 70% of the blade span. To align with the structural characteristics of the WT,

187 the airfoil for the WT is chosen based on approximately 70% of the actual owl wing (Arm
188 wing). The selected positions of the airfoils are approximately consistent with the minimum
189 locations in the OASPL curve. Consequently, the airfoil of the last section is selected as the tip
190 airfoil for the wind turbine. Wolf and Konrath [30] conducted measurements of the three-
191 dimensional shape of an owl's wing during a flapping cycle. The airfoils derived from the wings
192 of the taxidermy owl examined in this study closely resemble the configuration observed
193 during the gliding phase at a position approximately 5 meters along the right-to-left flight
194 direction. Furthermore, as shown in Figure 5b, these acquired airfoil profiles were utilized to
195 create various sections of the ducted wind turbine. These airfoils were subsequently
196 proportionally scaled and adjusted according to the specifications outlined in Table 2 to align
197 with the design requirements of the desired wind turbine. The ducted wind turbine is designed
198 based on the owl's wing but with some modifications to improve the noise reduction for urban
199 installations.

(a)   (b)
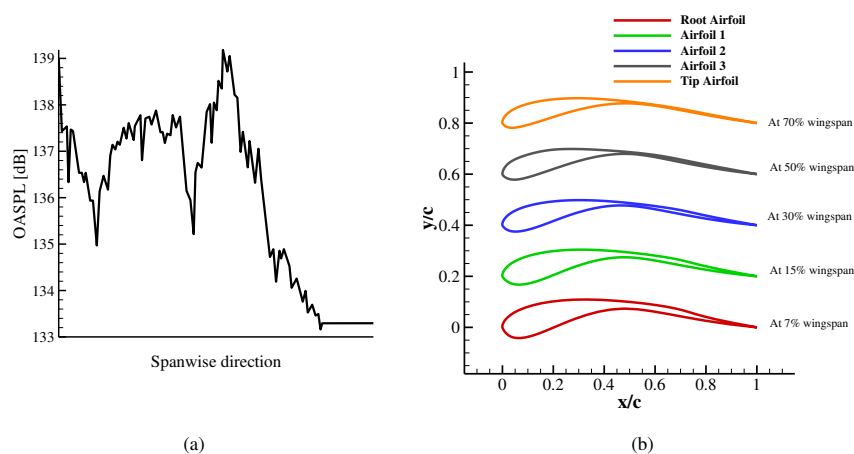
200   Figure 5: (a) the distribution curve of OASPL in the spanwise direction and illustrating the definition of the
201   position of the selected airfoils, (b) Airfoils section inspired by owl wings.

202 As depicted in Figure 6, the airfoils for various sections draw inspiration from owl wings in
203 shaping the desired geometry (refer to Table 2). Within the framework of DWT blade design,
204 a consistent airfoil is established within each of the delineated sections. However, to seamlessly
205 interlink these sections, the loft feature is implemented in CAD Software, allowing for
206 adaptable variation of the airfoil along the span. The turbine has a duct length of 1 meter and
207 an internal diameter of 1.6 meters.

7
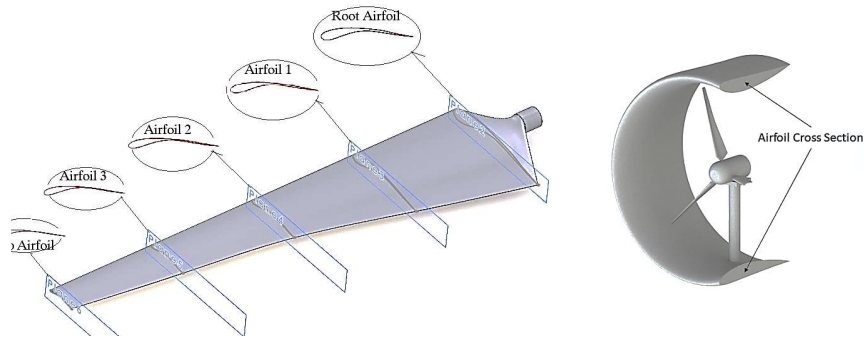
208   Figure 6: Schematic of the ducted wind turbine and multi-section blade.

209   Table 2: Design Features of Turbine.

Airfoils	Chord (m)
Root Airfoil	0.16
Airfoil 1	0.12
Airfoil 2	0.08
Airfoil 3	0.06
Tip Airfoil	0.04
Duct Airfoil	1

210   **Cases examined**

211   This research involved two simulations, which are described in brief below. In this
212   simulation, unsteady, compressible conditions are used in conjunction with LES turbulence
213   model and FW-H acoustic analogy.

214   1. Case 1: (Benchmark Blade- DonQi® wind turbine [31]).

215   2. Case 2: (Multi-section Blade) Use of airfoils of different sections of the owl wing
216   for blade sections: This case was done to investigate the effect of changing the
217   airfoil and the use of airfoils of different sections of the owl wing in different
218   sections of the blade.

219   **Governing equations**

220   This study utilized computational fluid dynamics with the Large Eddy Simulation (LES)
221   method for fluid flow analysis and the Ffowcs Williams and Hawkings (FW–H) acoustic
222   analogy for acoustic analysis. The governing equations for each method are detailed below.

223   **Fluid dynamics**

224   Turbulent flows are characterized by eddies with a wide range of length and time scales. In the
225   Large Eddy Simulation (LES) method, large eddies are solved directly and small eddies are
226   also modeled. The governing equations employed for LES are obtained by filtering the time-
227   dependent Navier-Stokes equations in either Fourier (wave-number) space or configuration
228   (physical) space. Filtering the Navier-Stokes equations, one obtains [32]:

8

$$\frac{\partial \rho}{\partial t} + \frac{\partial}{\partial x_i}\left(\rho \overline{u_i}\right) = 0 \tag{1}$$

229 And

$$\frac{\partial}{\partial t}\left(\rho \overline{u_i}\right) + \frac{\partial}{\partial x_j}\left(\rho \overline{u_i u_j}\right) = \frac{\partial}{\partial x_j}\left(\mu \frac{\partial \sigma_{ij}}{\partial x_j}\right) - \frac{\partial \overline{p}}{\partial x_i} - \frac{\partial \tau_{ij}}{\partial x_j} \tag{2}$$

230 where u, ρ, μ and p are the fluid velocity, density, turbulent viscosity, and static pressure,

231 and i and j are the subscripts with 1 and 2 for the x and y directions. Also, σ_{ij} is the stress

232 tensor due to molecular viscosity and τ_{ij} is the subgrid-scale stress.

233 **Acoustics**

234 Lighthill proposed the theory of the difference between real flow and reference flow and called

235 it analogy. Ffowcs Williams-Hawkings (FW-H) then challenged it and used to give solutions

236 to Lighthill's equation for a medium that includes moving surfaces and convected turbulent

237 flow. In this research, FW-H formulation has been used to model the propagation of sound

238 from a moving source [33, 34].

$$\frac{1}{c_\infty^2}\frac{\partial^2 p'}{\partial t^2} - \frac{\partial^2 p'}{\partial x_i^2} = \frac{\partial^2}{\partial x_i \partial x_j}\left\{T_{ij}H(f)\right\} - \frac{\partial}{\partial x_i}\left\{\left[P_{ij}n_j + \rho u_i\left(u_n - v_n\right)\right]\delta(f)\right\}$$
$$+ \frac{\partial}{\partial t}\left\{\left[\rho_\infty v_n + \rho\left(u_n - v_n\right)\right]\delta(f)\right\} \tag{3}$$

239 Where u_n and u_i are the fluid velocity in the normal direction of the integration surface and

240 in x_i direction, respectively. v_n and v_i represent the normal velocity of the integration surface

241 and the surface velocity component in x_i direction. $H(f)$ is Heaviside function and $\delta(f)$ is

242 Dirac delta function. p' is sound pressure in the far field ($p' = p - p_\infty$), n_j normal vector

243 pointing to the external area ($f > 0$), c_∞ is speed of sound in the far field, P_{ij} is compressive

244 stress tensor and T_{ij} is the Lighthill's stress tensor, given by:

$$T_{ij} = \rho v_i v_j + p_{ij} - \left(\rho - \rho_\infty\right)c_\infty^2\delta_{ij} \tag{4}$$

245 To solve Equation (3), the Green's function must be used to the open area. The complete

246 solution involves the calculation of surface and volume integrals, the first representing

247 monopole, dipole, and partially quadrupole acoustic sources, and the second representing

248 quadrupole sources in the area outside of the source surface. The volume integral becomes

249 negligible when the Mach number value of the flow is small and the source area covers the

250 source area. In Ansys Fluent, choosing a source on a solid surface-like rotor, the volume

251 integrals are neglected, and then the equation takes the following form [35]:

9

$$p'\left(\vec{x},t\right) = p'_T\left(\vec{x},t\right) + p'_L\left(\vec{x},t\right) \tag{5}$$

252 In equation (5), t is the observer time, $\vec{x}$ is the receiver position. The subscripts T and L. L

253 refer to the thickness (monopole) and loading (dipole) components, respectively and are given

254 as follows [33, 34]:

$$4\pi p'_T\left(\vec{x},t\right) = \int_{f=0}\left[\frac{\rho_\infty\left(\dot{U}_n + U_{\dot{n}}\right)}{r\left(1-M_r\right)^2}\right]ds + \int_{f=0}\left[\frac{\rho_\infty U_n\left(r\dot{M}_r + c_\infty\left(M_r - M^2\right)\right)}{r^2\left(1-M_r\right)^3}\right]ds \tag{6}$$

$$4\pi p'_L\left(\vec{x},t\right) = \frac{1}{c_\infty}\int_{f=0}\left[\frac{\dot{L}_r}{r\left(1-M_r\right)^2}\right]ds + \int_{f=0}\left[\frac{L_r - L_M}{r\left(1-M_r\right)^2}\right]ds$$
$$+ \frac{1}{c_\infty}\int_{f=0}\left[\frac{L_r\left\{rM_r + c_\infty\left(\dot{M}_r - M^2\right)\right\}}{r^2\left(1-M_r\right)^3}\right]ds \tag{17}$$

255 Where:

256
$$U_i = v_i + \frac{\rho}{\rho_\infty}\left(u_i - v_i\right)$$
$$L_i = P_{ij}\hat{n}_j + \rho u_i\left(u_n - v_n\right)$$

257 Where M and r represent the surface velocity vector and the unit radiation vector. The two

258 terms $p'_T\left(\vec{x},t\right)$ and $p'_L\left(\vec{x},t\right)$ in Equation (5) are referred to as thickness and loading terms,

259 respectively.

260 **Numerical solver**

261 The commercial software ANSYS-FLUENT has been used for all simulations carried out in

262 this work. For an accurate calculation of the flow field around the blade, the LES solution was

263 calculated with the Fluent SIMPLE solver. This approach has been proven suitable to describe

264 similar problems in wind turbines. This solver used the finite volume method as a discretization

265 procedure with Bounded Central Differences for momentum and Second Order Central

266 Differences for pressure. A Bounded Second Order Implicit scheme is used for the time

267 marching method in the present work as a temporal discretization scheme with the convergence

268 criteria of 10^{-4}. Since the Mach number at the blades of a wind turbine is always less than 0.2,

269 the air has been modeled as incompressible for reducing the computational costs while

270 maintaining accuracy.

10

271   The 3D mesh of the full rotor was carried out first by drawing it in the SpaceClaim software,
272   while the mesh generation was performed using Fluent Meshing. For this problem, a
273   polyhexcore mesh is generated. The computational domain is divided into two parts: the
274   internal rotating field and the external relatively stationary flow field. The interfaces are set to
275   transfer data between the rotational and stationary parts. Coupled problems between the two
276   parts have a significant influence on the accuracy of numerical simulation. In the present study,
277   the sliding mesh model is used to account for the rotation of the blades.

278   Figure 7 shows the boundary conditions, including velocity inlet and pressure outlet boundaries
279   used to simulate the far field flow. In this case, the velocity of the free stream is 5 m/s,
280   corresponding to the Reynolds number (Re) based on the duct chord length c (Re=$3.4*10^5$).
281   The rotational speed of the wind turbine is 39.84 rad/s. distance from the main inlet boundary
282   to the leading edge of the blade is 10×c and the distance from the leading edge to the main
283   outlet boundary is 20×c.
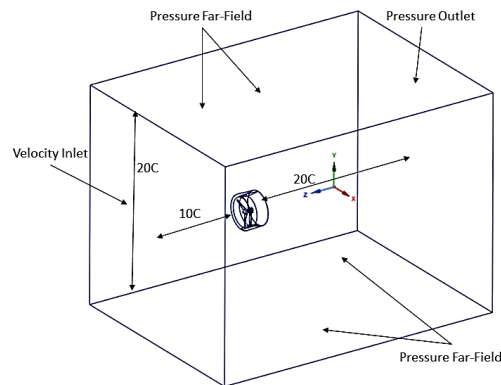
284

285   Figure 7: Computational domain used for the LES simulation. The length is indicated in terms of duct chord
286   length c.

287   According to Figure 8, the computational domain is discretized by about 6 million cells. The
288   fine mesh is used on the whole rotor surface and gradually becomes coarser as the distance
289   from the blades increases. Technique based on the previous results of k-epsilon turbulence
290   model have been used to evaluate the grid resolution in LES method. In this technique,
291   parameter f, has been calculated for the entire computing field by RANS model. The parameter
292   f denotes the ratio of the integral turbulence length scale to the filter width. This can be
293   simplified and expressed as f $= k^{\wedge 3/2}$ / ($\varepsilon \times$ (Cell Volume)$^{\wedge 1/3}$), where k represents kinetic
294   energy and ε signifies turbulent dissipation [36]. In most areas, this value is of the order of 5-
295   10, which indicates the good quality of the mesh. Therefore, the grid resolution meets the
296   requirements for the LES calculation.

11

| (a) | (b) |
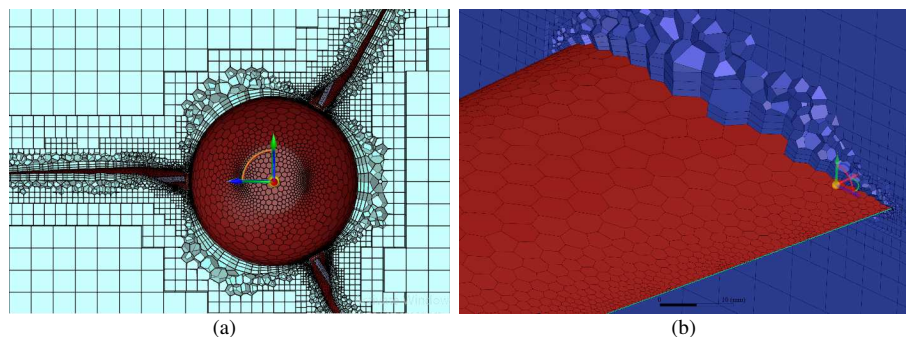
297 Figure 8: Schematic view of the computational domain. (a) Front view of DWT and (b) Side view of the blade.

298 **Results and Discussion**

299 **Validation**

300 The validation method for this research was conducted with great attention to details. It
301 involved a rigorous comparison between the thrust force coefficient (C_T), which is derived
302 from the pressure coefficient (Cp) along the chord, and the reference data obtained from Ten
303 Hoopen's study described in reference [37]. The main objective was not to precisely reproduce
304 the Cp values at each location on the surface along the chord, but rather to guarantee that the
305 general pattern of Cp distribution closely corresponds to the reference, as illustrated in Figure
306 9. The key element of our validation process involved comparing the precise values of C_T, with
307 a specific emphasis on the correlation between the thrust ratio in our simulation and the
308 reference of [37].

309 It is important to note that Ten Hoopen's work lacks detailed information regarding the
310 manufacturing accuracy of the model and the precision of the measuring instruments. This
311 implies that achieving a precise match for local Cp values between the simulated results and
312 the reference data may not be possible. Hence, our validation focused on confirming the pattern
313 of behavior and the distribution curve of pressure.

314 In the present context, the validation of the simulation, which relies on the Donqi blade results
315 and is supplemented by the experimental findings of Ten Hoopen [37], demonstrates a
316 fundamental similarity in pressure distributions. However, there are slight variations observed
317 in the vicinity of the suction peak region, which may be attributed to assumptions made during
318 the simulation or inherent uncertainties in the experimental data. This validation verifies that
319 the aerodynamic characteristics of the ducted wind turbine (DWT) are accurately represented
320 and simulated, especially when examining how the pressure distributions react to different
321 wake propagation velocities (V_w), which in turn affect the maximum absolute pressures on
322 various sides of the airfoil. Therefore, the duct thrust force coefficient (C_T) has played a crucial
323 role in our work by calculating the grid resolution and assessing the aerodynamic changes in
324 the DWT models. This ensures that our technique closely matches the established experimental
325 standards. Table 3 presents a comparison of various grids against experimental and numerical

12

326   results. The table indicates that the error for the 6 million grid was kept below 10%, meeting
327   the required accuracy standards. Therefore, the chosen grid number for this study was 6
328   million. The multi-section blade exhibited a 6.4 % increase in thrust force coefficient compared
329   to the conventional blade.

330

Table 3: Comparison of the thrust force coefficient.

	Experimental Value [37]	2.7 million numerical value (Benchmark)	LES Error (%)	4.3 million numerical value (Benchmark)	LES Error (%)	6 million numerical value (Benchmark)	LES Error (%)	6 million numerical value (Multi-section)	Difference Value (percentage increase)
thrust force coefficient, C_T	0.689	0.811	17.7	0.773	12.2	0.735	6.7	0.782	6.4
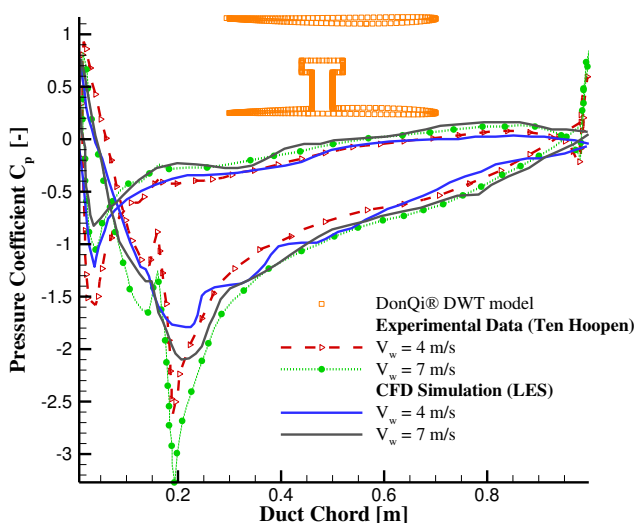
331
332   Figure 9: Comparison between numerical and experimental solution of pressure distribution.

333   To validate the acoustic findings in our present study, we have conducted a comparative
334   analysis of the Power Spectral Density graph of the acoustic pressure, focusing on the blade
335   passing frequency, as illustrated in Figure 10. This evaluation was undertaken at the
336   microphone location set at 90 degrees for the DonQi® DWT model, as examined by Dighe et
337   al, [31]. It's evident that minimal deviations exist for blade passing frequencies below 2, with
338   more pronounced discrepancies emerging at higher frequencies. Overall distribution has
339   similar characteristic which the 2nd harmonic is less pronounced, and the 4th harmonic stronger.
340   Importantly, our LES approach not only captures these variations but also effectively
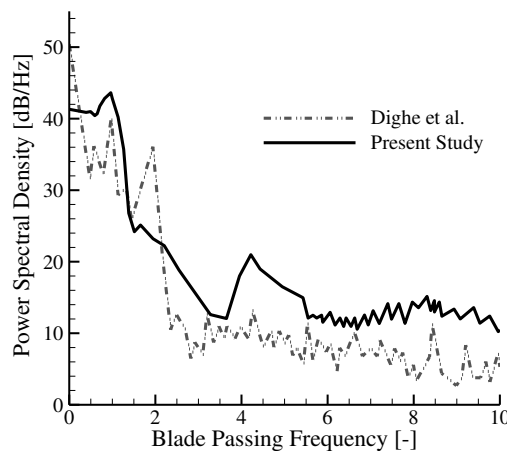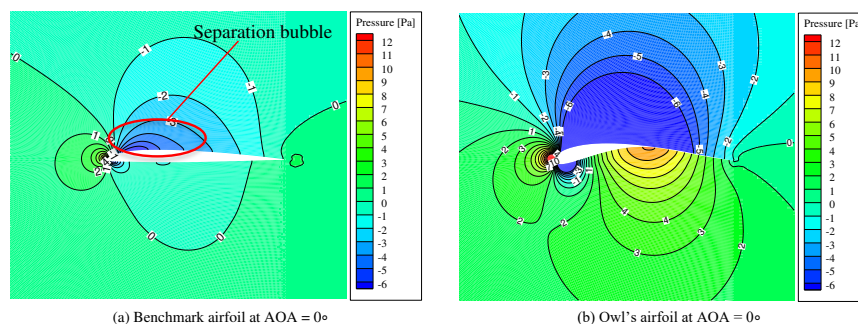341   characterizes the transitional trends.

13

342
343 Figure 10: Validating Acoustic Results.

344 **Aerodynamics results**

345 This section focuses on the analysis of the characteristic of the owl airfoil compared to a
346 conventional airfoil in a 2D context used for wind turbine. The evaluation is carried out by
347 analyzing the aerodynamic properties of both types of airfoils, and the results are discussed in
348 this section.

349 Figure 11 illustrate the pressure contour for the owl and benchmark airfoils at angles of attack
350 of 0 and 6 degrees. The unique shape of the owl airfoil, characterized by a thicker leading edge,
351 higher curvature, and thinner trailing edge, generates a separation bubble. More pronounced in
352 the owl airfoil Compared to a standard reference, leading to a more significant pressure
353 difference and, in turn, increased lift (as depicted in Figure 12).

(a) Benchmark airfoil at AOA = 0°

(b) Owl's airfoil at AOA = 0°

14

(c) Benchmark airfoil at AOA = 6°   (d) Owl's airfoil at AOA = 6°

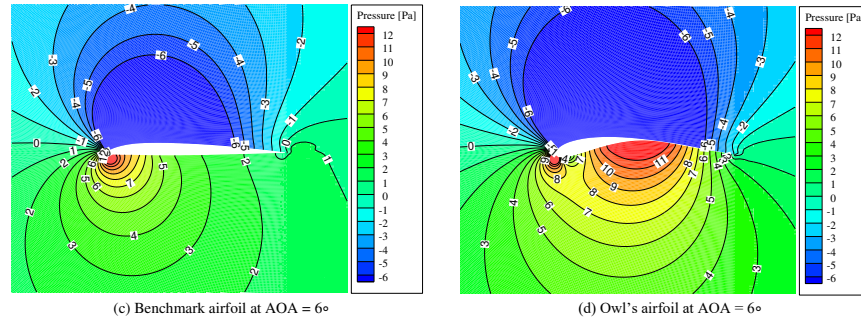354   Figure 11: The pressure contour at different angles of attack.

355
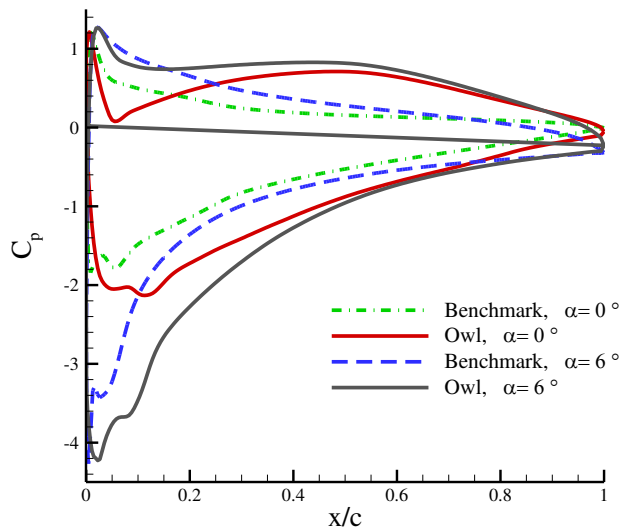356   Figure 12: Cp comparison between Owl and benchmark airfoils for AOA= 0° and AOA= 6°.

357   In the owl airfoil, the blade's maximum camber, maximum thickness, and their respective
358   positions are altered, enhanced lift performance, increasing the maximum lift coefficient from
359   1.8 to 2.8 and raising the stall angle of attack from 12° to 14° (as shown in Figure 13a). While
360   the drag coefficient is higher for low attack angles in the owl airfoil, resulting in increased
361   drag, this is a necessary tradeoff for generating more lift (as shown in Figure 13b). However,
362   as shown in Figure 13c, the owl airfoil consistently outperforms the conventional airfoil in
363   terms of lift to drag ratio all angles of attack. There is a noticeable improvement in the lift-to-
364   drag ratio when the angle of attack reaches 5 degrees. Between angles of 8 to 10 degrees, the
365   aerodynamic performance remains relatively stable. However, beyond this range, in all
366   sections, there appears to be a decline in performance, possibly attributed to an increase in drag.

15

(a)

(b)

(c)
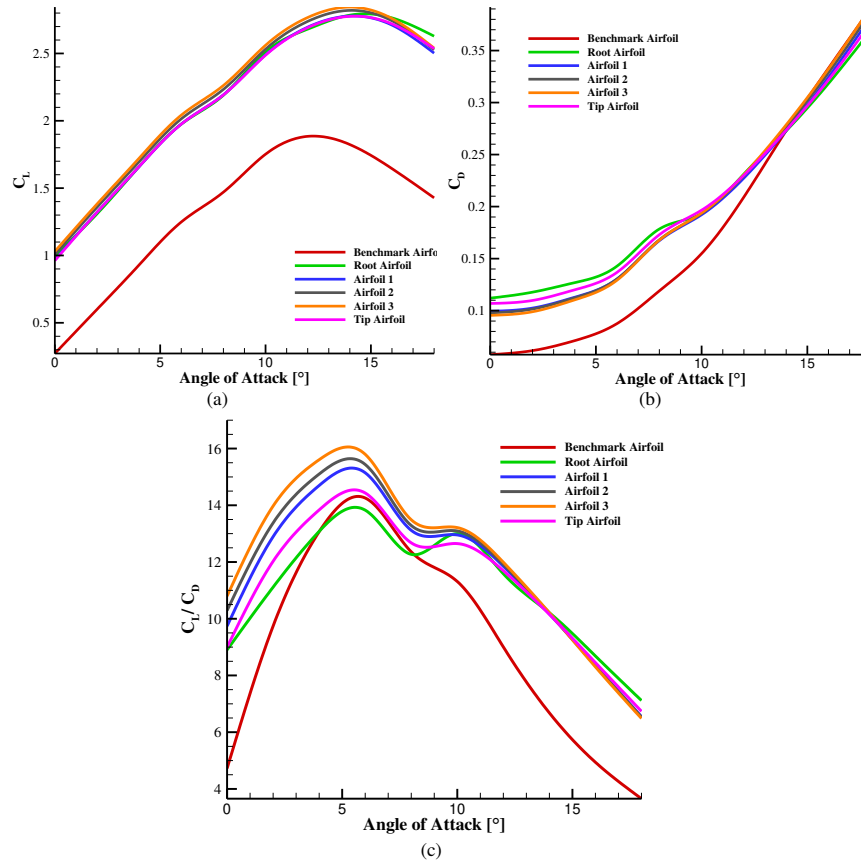
Figure 13: (a) Lift coefficients, (b) Drag coefficients and (c) Lift-to-drag ratio (Cl/Cd) curves of the airfoils at different AOA.

This section explores and presents the aerodynamic features of the turbine after the integration of the owl airfoil. The implementation of the owl airfoil on the turbine is carried out, and the resultant aerodynamic properties are studied and analyzed.

To better illustrate the changes in the flow field and interactions between the turbine and the boundary layer as a result of the inlet flow, a 2D section of the flow velocity is shown in the XY plane in Figure 14a. As can be seen, there are areas of low speed around the duct and turbine holder. At the same time, there are also high-speed areas at the ends of the blades and downstream (in the wake) which is 25 m/s. This indicates that the duct acts as a diffuser and increases the speed of the incoming air.

For Case 2, the instantaneous flow fields around the ducted wind turbine are shown using the Q criterion in Figure 14b. The figure illustrates the formation of vortices on the inner wall of

16

380 the duct. Due to the increase in camber and changes in the thickness of the airfoil as the flow
381 moves along the inner wall of the duct, the speed of the flow increases. The front vortices
382 originate from the starting point of the inner side of the duct and adopt a helical shape as they
383 get closer to the turbine. Consequently, this leads to an increase in turbulence structures and an
384 increase in Turbulence Intensity (TI), which ultimately breaks up the larger front vortices into
385 smaller ones. It also shows that the LES turbulence model predicts the turbulence fluctuations
386 around a DWT well and provides a clearer picture of the complex flows around the turbine.

(a)   (b)
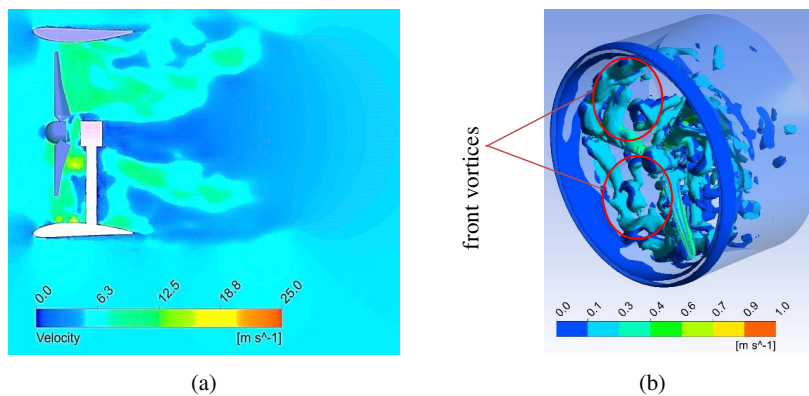
387   Figure 14: (a) Velocity contour, (b) Q criterion.

388 In the context of a wind turbine, the conversion of mechanical energy into electrical energy
389 hinges on the performance of the aerodynamic system, quantified as the power coefficient
390 (C_{PWR}). In parallel, an essential factor in the design of turbine blades is the Tip Speed Ratio
391 (TSR), representing the ratio between the linear speed of the blade tip and the wind speed.
392 Consequently, this section delves into the variations in the power coefficient concerning TSR
393 for both benchmark and multi-section blades. As illustrated in Figure 15, C_{PWR} exhibits a non-
394 linear relationship with TSR, with the maximum C_{PWR} value occurring at TSR = 8 in both
395 cases. This maximum value signifies the peak efficiency of the DWT. Thus, the selection of
396 the optimal TSR value is of paramount importance. Furthermore, as depicted in the figure 15,
397 for TSR values below 5, there is negligible discrepancy in C_{PWR} between the two blade types,
398 with their performance differing by less than 10%. However, as TSR values increase, the C_{PWR}
399 parameter demonstrates a significant rise, underscoring the benefit of employing multi-section
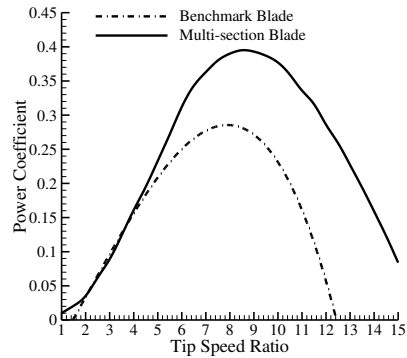400 blades.

17

401

402 Figure 15: Variation in Power Coefficients for Benchmark and Multi-Section Blades across Various Tip Speed
403 Ratio.

404 **Aeroacoustics results**

405 To investigate the sound around the turbine, according to Figure 16, thirty receivers are being
406 used in the current study. The receivers are positioned at a distance of 1.5 times the chord
407 length of the Duct airfoil. Receivers are spaced 12 degrees apart.
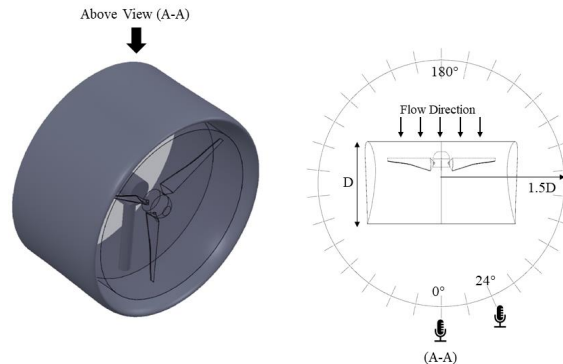

408
409 Figure 16: Receivers position.

410 Based on the receiver position curve, two specific points are analyzed in this study, point 1 at
411 0 degrees and point 2 at 24 degrees. Figure 17 displays sound pressure level graphs for both
412 points, showing the frequency response for two cases. By implementing owl wing airfoils,
413 noise generated by free stream turbulence and trailing edge noise is reduced. Notably, this
414 improvement has the most significant impact on higher frequencies. The multi-section results
415 suggest that owl-inspired airfoils have proven effective in mitigating noise.

416 According to the polar curve of Overall Sound Pressure Level (OASPL), as shown in Figure
417 18 based on the position of the receivers, it can be seen that the use of airfoils of owl-inspired
418 reduces the sound by an average of 6-8 decibels at 60 to -60 degrees (which represents the flow

18

419 exit area from the duct). As can be seen, in some positions, including 90 and 270 degrees, there
420 is no change in the OASPL curve for owl-shaped wing (multi-section blade). It does not reduce
421 sound in the radial direction. As a result, to reduce sound, it is recommended to make changes
422 such as using perforated plates in the structure of the duct and its surfaces, as well as adding
423 sound-absorbing materials inside.

(a)   (b)
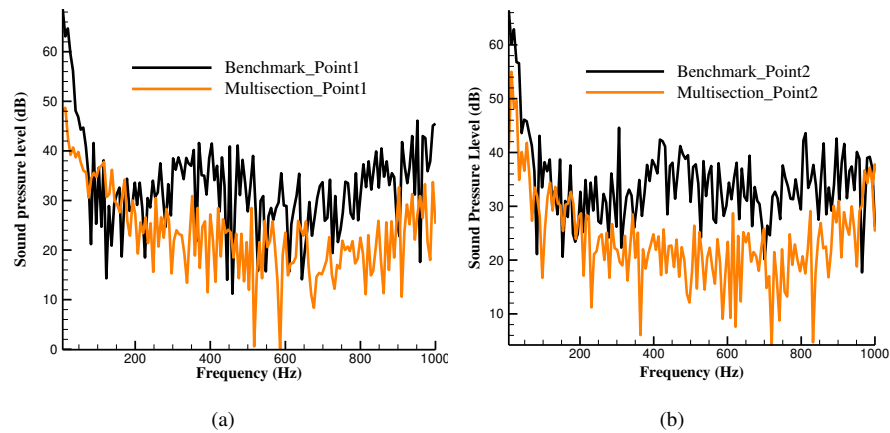
424   Figure 17: Comparison between SPL vs Frequency of 2 cases study at point1 (a) and point2 (b).
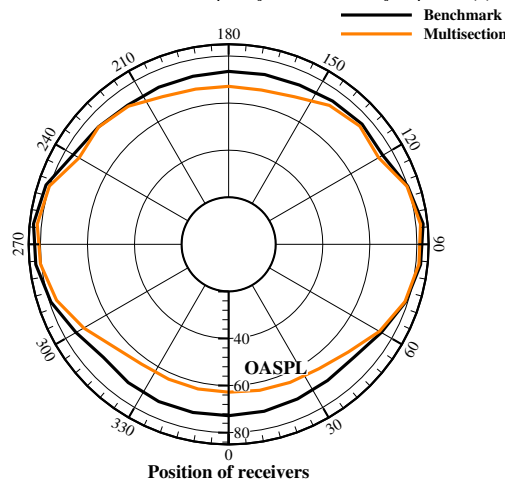

425
426   Figure 18: Comparison between SPL of 2 cases study around the ducted.

427 As can be seen in Figure 19a, the highest sound pressure level occurs on the inner surface of
428 the duct which the lowest level is on the outer surfaces of the duct. The highest SPL value on
429 the inner surface of the duct is typically associated with the airfoil's thickest portion located at
430 the leading edge. As a result, the use of a duct as a diffuser cover significantly reduces the
431 sound and act as a barrier, as well as protect the surrounding environment from damage. Based

19

AIP
Publishing

432   on the contour presented in figure 19b, it appears that altering the blade foils did not result in
433   any detrimental impact on the level of noise produced at the tip of the turbine duct. Also, figures
434   19 illustrates how the surface under the airfoil, which is the suction area, has a more significant
435   effect on noise production. An explanation for this can be found in the change in the camber
436   line and the changes in the thickness of the airfoil. Therefore, it leads to an increase in
437   turbulence structures and pressure fluctuations, resulting in more sound being produced on the
438   lower surface of the airfoil. With comparing Figures 19a and 19b, it becomes apparent that the
439   SPL value has decreased both downstream and on the inner surface of the duct. Further analysis
440   can be conducted by referring to Figure 19c, which illustrates sound pressure levels specifically
441   along the inner surface of the duct. In this segment, a section is formed on the interior of the
442   duct. It is worth noting that modifications made to the turbine blade have a noticeable effect on
443   the noise generated downstream, leading to a reduction in noise at the trailing edge of the inner
444   duct. This noise reduction is approximately equal to 10 dB in all positions after the turbine
445   tower. Intriguingly, the use of multi-section blades does not impact the noise levels in front of
446   the rotor.
447
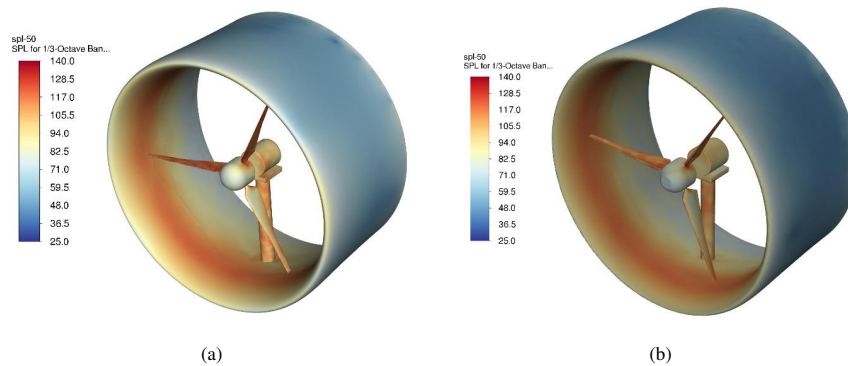
(a)   (b)

(c)
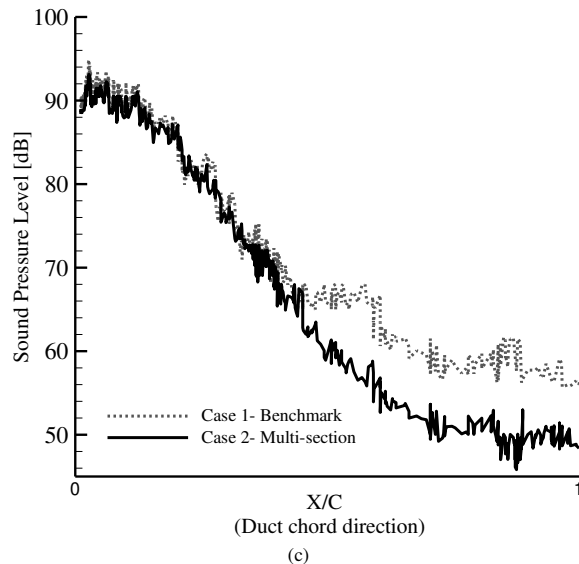
448   Figure 19: Noise level contour for frequency 50 Hz for cases number 1 (a) and 2 (b) and (c) Comparative
449   Analysis of Sound Pressure Levels along the Inner Duct Surface between Cases 1 and 2.

450   Upon analyzing the frequencies ranging from 50 Hz to 500 Hz in case number 2 as shown in
451   Figure 20, it becomes apparent that noise levels decrease as the frequency increases. The
452   maximum noise production within the duct occurs in the regions near the leading edge to the
453   tower, with the highest levels of noise generated in the corresponding areas of the blade tips.
454   Also, this figure indicates that the most effective place to reduce noise is this area, which is the
455   logical point to consider the perforated plate (punch) along with the absorber at the position of
456   the inner junction to the turbine tower to the duct.
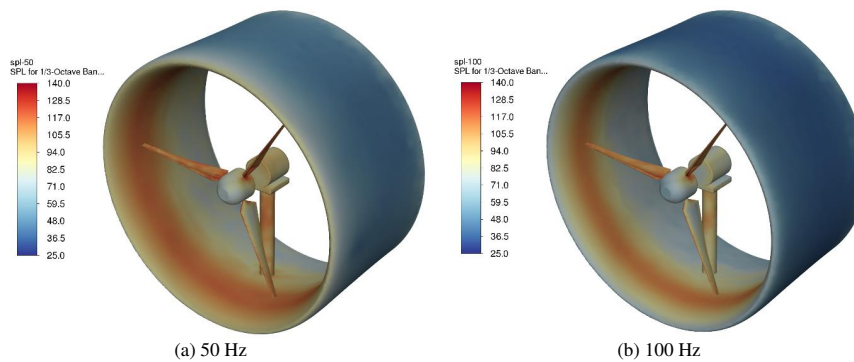
(a) 50 Hz
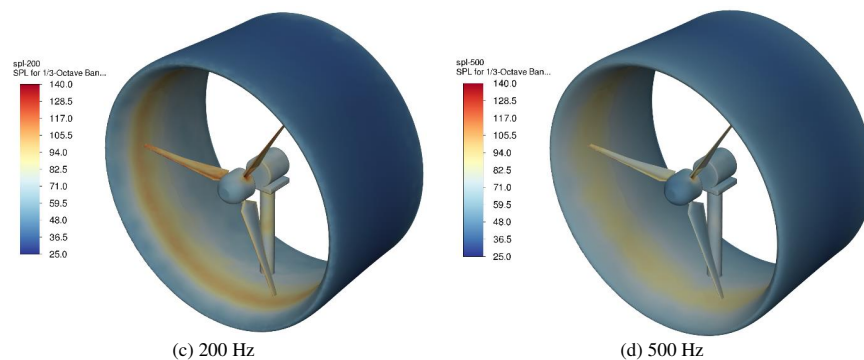
(b) 100 Hz

(c) 200 Hz   (d) 500 Hz

457   Figure 20: Noise level contour for frequencies 50 Hz to 500 Hz for case number 2.

458   **Conclusions**

459 In this comprehensive study, we have employed advanced Large Eddy Simulation (LES)
460 turbulence modeling and Ffowcs Williams-Hawkings (FW-H) acoustic analogy to
461 meticulously analyze the aeroacoustic and aerodynamic properties of ducted wind turbine
462 blades. These blades are innovatively designed, drawing inspiration from the silent flight
463 mechanism of owl wings. Our primary aim was to address the critical challenge of reducing
464 aerodynamic noise, particularly the noise generated by inflow turbulence and trailing edges,
465 while concurrently ensuring that the aerodynamic performance remains uncompromised.
466 The investigation revealed that the incorporation of bio-inspired airfoil sections, meticulously
467 derived from owl wings through 3D scanning techniques, significantly influences the noise
468 reduction and aerodynamic efficiency of wind turbines. Specifically, the application of these
469 uniquely designed airfoils resulted in a notable reduction of aerodynamic noise by
470 approximately 8 decibels, which translates to an improvement of about 12% when compared
471 to conventional designs. This achievement underscores the potential of bio-inspired
472 modifications in enhancing the environmental compatibility of wind turbines, particularly in
473 urban settings where noise pollution is a significant concern.
474 Moreover, our results demonstrated a 6.4% increase in the thrust force coefficient for the multi-
475 section blade compared to the conventional blade design. The power coefficient analysis
476 further revealed that the maximum power coefficient occurred at a Tip Speed Ratio (TSR) of
477 8 for both the benchmark and multi-section blades, emphasizing the optimized aerodynamic
478 efficiency achieved through the bio-inspired design.
479 Furthermore, our study delved into the aeroacoustic performance, where the findings indicated
480 a substantial noise reduction in specific areas around the duct, especially downstream and on
481 the inner surface. These results suggest that the strategic implementation of owl-inspired airfoil
482 profiles not only benefits the noise profile but also contributes to the overall aerodynamic
483 efficiency of the turbine. However, it's worth noting that the radial sound suppression remained
484 unaffected, suggesting additional avenues for enhancing the aeroacoustic performance,
485 possibly through further structural modifications or the integration of sound-absorbing
486 materials.
487 In conclusion, this research not only contributes valuable insights into the aeroacoustic and
488 aerodynamic optimization of wind turbines but also highlights the potential of bio-inspired
489 designs in the field of renewable energy. The significant reduction in noise levels, coupled with
490 the maintenance of aerodynamic performance, presents a compelling case for the adoption of

491 such innovative design strategies in future wind turbine development, particularly in noise-
492 sensitive environments. Our findings lay a solid foundation for future studies and the practical
493 application of bio-inspired designs in enhancing the sustainability and community acceptance
494 of wind energy solutions.

495 **Data Availability**

496 The data used to support the findings of this study are available from the corresponding author
497 upon request.

498 **Conflicts of Interest**

499 The authors declare that there is no conflict of interest regarding the publication of this paper.

500 **Funding Statement**

501 The authors have no relevant financial or non-financial interests to disclose.

502 **Acknowledgments**

506 **References**

507 [1]   A.H. Butt, B. Akbar, J. Aslam, N. Akram, M.E.M. Soudagar, F.P.G. Márquez, M.Y. Younis, E. Uddin,
508   "Development of a linear acoustic array for aero-acoustic quantification of camber-bladed vertical axis
509   wind turbine," Sensors (Switzerland), vol. 20, pp. 1-17, 2020.
510 [2]   M. Ilie, J.W. McAfee, "Aerodynamics and design of vertical-axis wind turbine; numerical studies using
511   les and iddes," in AIAA AVIATION 2020 FORUM, 2020, pp. 1-9.
512 [3]   T. Fukano, C.-M. Jang, "Tip clearance noise of axial flow fans operating at design and off-design
513   condition," Journal of sound and vibration, vol. 275, pp. 1027-1050, 2004.
514 [4]   H. Weger, M. Weger, M. Klaas, W. Schröder, "Features of owl wings that promote silent flight,"
515   Interface Focus, vol. 7, 2017.
516 [5]   R. Graham, "The silent flight of owls," The Aeronautical Journal, vol. 38, pp. 837-843, 1934.
517 [6]   E. Mascha, "Über die schwungfedern," Zeitschrift für wissenschaftliche Zoologie, vol. 77, pp. 606-651,
518   1904.
519 [7]   L. Wang, X. Liu, D. Li, "Noise reduction mechanism of airfoils with leading-edge serrations and surface
520   ridges inspired by owl wings," Physics of Fluids, vol. 33, 2021.
521 [8]   R. Hayden, "Reduction of noise from airfoils and propulsive lift systems using variable impedance
522   systems," in 3rd AIAA Aeroacoustics Conf., Palo Alto, CA, USA, 1976.
523 [9]   P. Chaitanya, P. Joseph, S. Narayanan, C. Vanderwel, J. Turner, J.-W. Kim, B. Ganapathisubramani,
524   "Performance and mechanism of sinusoidal leading edge serrations for the reduction of turbulence–
525   aerofoil interaction noise," Journal of Fluid Mechanics, vol. 818, pp. 435-464, 2017.
526 [10]   B.Y. Zhou, S.R. Koh, N.R. Gauger, M. Meinke, W. Schöder, "A discrete adjoint framework for trailing-
527   edge noise minimization via porous material," Computers & Fluids, vol. 172, pp. 97-108, 2018.
528 [11]   C. Pimenta, W.R. Wolf, A.V. Cavalieri, "A fast numerical framework to compute acoustic scattering by
529   poroelastic plates of arbitrary geometry," Journal of Computational Physics, vol. 373, pp. 763-783, 2018.
530 [12]   J.M. Turner, J.W. Kim, "Aeroacoustic source mechanisms of a wavy leading edge undergoing vortical
531   disturbances," Journal of Fluid mechanics, vol. 811, pp. 582-611, 2017.
532 [13]   E. Sarradj, C. Fritzsche, T. Geyer, "Silent owl flight: Bird flyover noise measurements," AIAA journal,
533   vol. 49, pp. 769-779, 2011.
534 [14]   K. Lee, Y. Kozato, S. Kikuchi, S. Imao, "Numerical simulation of flow control around a rectangular
535   cylinder by dielectric barrier discharge plasma actuators," Physics of Fluids, vol. 34, 2022.

536   [15]   E. Fatahian, F. Ismail, M.H.H. Ishak, W.S. Chang, "Aerodynamic performance improvement of savonius
537   wind turbine through a passive flow control method using grooved surfaces on a deflector," Ocean
538   Engineering, vol. 284, p. 115282, 2023.
539   [16]   F. Eydi, A. Mojra, R. Abdi, "Comparative analysis of the flow control over a circular cylinder with
540   detached flexible and rigid splitter plates," Physics of Fluids, vol. 34, 2022.
541   [17]   W. Song, Z. Mu, Y. Wang, Z. Zhang, S. Zhang, Z. Wang, B. Li, J. Zhang, S. Niu, Z. Han, "Comparative
542   investigation on improved aerodynamic and acoustic performance of abnormal rotors by bionic edge
543   design and rational material selection," Polymers, vol. 14, p. 2552, 2022.
544   [18]   T. Liu, K. Kuykendoll, R. Rhew, S. Jones, "Avian wing geometry and kinematics," AIAA journal, vol.
545   44, pp. 954-963, 2006.
546   [19]   S. Klaÿ, T. Bachmann, M. Klaas, H. Wagner, W. Schröder, "Experimental analysis of the flow field over
547   a novel owl based airfoil," Animal Locomotion, pp. 413-427, 2010.
548   [20]   T. Bachmann, G. Mühlenbruch, H. Wagner, "The barn owl wing: An inspiration for silent flight in the
549   aviation industry?," in Bioinspiration, Biomimetics, and Bioreplication, 2011, pp. 142-155.
550   [21]   T. Geyer, E. Sarradj, C. Fritzsche, "Silent owl flight: Acoustic wind tunnel measurements on prepared
551   wings," in 18th AIAA/CEAS Aeroacoustics Conference (33rd AIAA Aeroacoustics Conference), 2012,
552   p. 2230.
553   [22]   K. Kondo, H. Aono, T. Nonomura, M. Anyoji, A. Oyama, T. Liu, K. Fujii, M. Yamamoto, "Analysis of
554   owl-like airfoil aerodynamics at low reynolds number flow," Transactions of the Japan Society for
555   Aeronautical and Space Sciences, Aerospace Technology Japan, vol. 12, pp. Tk_35-Tk_40, 2014.
556   [23]   W. Tian, Z. Yang, Q. Zhang, J. Wang, M. Li, Y. Ma, Q. Cong, "Bionic design of wind turbine blade
557   based on long-eared owl's airfoil," Applied Bionics and Biomechanics, vol. 2017, 2017.
558   [24]   M. Anyoji, S. Wakui, D. Hamada, H. Aono, "Experimental study of owl-like airfoil aerodynamics at low
559   reynolds numbers," Journal of Flow Control, Measurement & Visualization, vol. 6, p. 185, 2018.
560   [25]   F. Moslem, M. Masdari, K. Fedir, B. Moslem, "Experimental investigation into the aerodynamic and
561   aeroacoustic performance of bioinspired small-scale propeller planforms," Proceedings of the Institution
562   of Mechanical Engineers, Part G: Journal of Aerospace Engineering, vol. 237, pp. 75-90, 2023.
563   [26]   H. Aono, K. Kondo, T. Nonomura, M. Anyoji, A. Oyama, K. Fujii, M. Yamamoto, "Aerodynamics of
564   owl-like wing model at low reynolds numbers," Transactions of the Japan Society for Aeronautical and
565   Space Sciences, vol. 63, pp. 8-17, 2020.
566   [27]   M. Muthuramalingam, E. Talboys, H. Wagner, C. Bruecker, "Flow turning effect and laminar control by
567   the 3d curvature of leading edge serrations from owl wing," Bioinspiration & Biomimetics, vol. 16, p.
568   026010, 2020.
569   [28]   N. Ricks, P. Tsirikoglou, F. Contino, G. Ghorbaniasl, "A cfd-based methodology for aerodynamic-
570   aeroacoustic shape optimization of airfoils," in AIAA Scitech 2020 Forum, 2020, p. 1729.
571   [29]   H. Gruschka, I. Borchers, J. Coble, "Aerodynamic noise produced by a gliding owl," Nature, vol. 233,
572   pp. 409-411, 1971.
573   [30]   T. Wolf, R. Konrath, "Avian wing geometry and kinematics of a free-flying barn owl in flapping flight,"
574   Experiments in Fluids, vol. 56, pp. 1-18, 2015.
575   [31]   V.V. Dighe, F. Avallone, G. van Bussel, "Effects of yawed inflow on the aerodynamic and aeroacoustic
576   performance of ducted wind turbines," Journal of Wind Engineering and Industrial Aerodynamics, vol.
577   201, 2020.
578   [32]   K. Güzey, U.E. Aylı, E. Kocak, S. Aradag, "Investigation of aerodynamic and aeroacoustic behavior of
579   bio-inspired airfoils with numerical and experimental methods," Proceedings of the Institution of
580   Mechanical Engineers, Part C: Journal of Mechanical Engineering Science, p. 09544062231185495,
581   2023.
582   [33]   F. Eydi, A. Mojra, "A numerical study on the benefits of passive-arc plates on drag and noise reductions
583   of a cylinder in turbulent flow," Physics of Fluids, vol. 35, 2023.
584   [34]   Y. Wang, T. Mikkola, S. Hirdaris, "A fast and storage-saving method for direct volumetric integration
585   of fwh acoustic analogy," Ocean Engineering, vol. 261, p. 112087, 2022.
586   [35]   D. Romik, I. Czajka, "Numerical investigation of the sensitivity of the acoustic power level to changes
587   in selected design parameters of an axial fan," Energies, vol. 15, p. 1357, 2022.
588   [36]   S. Gant, "Practical quality measures for large-eddy simulation," in Direct and Large-Eddy Simulation
589   VII: Proceedings of the Seventh International ERCOFTAC Workshop on Direct and Large-Eddy
590   Simulation, held at the University of Trieste, September 8-10, 2008, 2010, pp. 217-222.
591   [37]   T. Hoopen, "An experimental and computational investigation of a diffuser augmented wind turbine:
592   With an application of vortex generators on the diffuser trailing edge," Ph.D. thesis, Delft University of
593   Technology, Delft, The Netherlands, 2009.

594